



Dalton
Transactions

Synthesis, photophysical characterization, and aerobic photoredox reactivity of electron-rich tellurorhodamine photocatalysts

| | |
|-------------------------------|---|
| Journal: | <i>Dalton Transactions</i> |
| Manuscript ID | DT-ART-11-2022-003534.R1 |
| Article Type: | Paper |
| Date Submitted by the Author: | 29-Jan-2023 |
| Complete List of Authors: | Rettig, Irving; Portland State University, Halvorsen, Kristine; Portland State University, Chemistry McCormick, T.; Portland State University, Chemistry |
| | |

SCHOLARONE™
Manuscripts

TITLE: Synthesis, photophysical characterization, and aerobic redox reactivity of electron-rich tellurorhodamine photocatalysts

Irving D. Rettig, Kristine M. Halvorsen, Theresa, M. McCormick*

Department of Chemistry, Portland State University, Portland, Oregon, 97201, USA

*t.m.mccormick@pdx.edu

ABSTRACT

Tellurorhodamine dyes are a class of self-sensitizing chromophores that we have previously shown can photocatalytically oxidize a variety of organic and inorganic compounds with visible light, oxygen, and water. A new series of tellurorhodamine chromophores containing electron donating moieties were synthesized to explore how different electron donating groups affects photophysical properties and catalyst function. The synthesized complexes **1B**, **1C**, and **1D** contain increasingly electron-donating substituents (Me, t-Butyl, OMe) on the xylene ring. **1A**, containing an unsubstituted xylene, was synthesized for use as a control. UV-Vis spectroscopy was used to determine the photophysical properties of the dyes and for kinetic and thermodynamic studies. With visible light irradiation all dyes could be oxidized at room temperature to their corresponding telluroxides **2A**, **2B**, **2C**, and **2D**, as confirmed by mass spectroscopy. Comparative reduction studies using our previously established silane oxidation reaction showed that decreasing the electron density of the xylene moiety increased the rate of reduction, corresponding to a decrease in the experimental ΔG . **2D** has the smallest energy barrier to silane oxidation and a linear increase in rate with increasing substituent electron withdrawing nature was observed at low temperatures, and non-linearity at high temperatures.

1 INTRODUCTION

Enrolling molecular oxygen in catalytic oxidation reactions is an important step in green methods development by replacing toxic chemical oxidants with environmentally neutral reagents.^{1,2} However, the spin forbidden nature of reactions involving triplet ground state dioxygen and singlet ground state organic substrates poses a major challenge to accessing facile reactivity.³ Organometallic catalysts have been shown to facilitate reactions of this type wherein dioxygen is used as an electron donor in the catalyst regeneration step following product elimination. Inspired by the industrially transformative Wacker process,^{4,5} Stahl and coworkers have extensively studied palladium catalysts in aerobic oxidation reactions.⁶⁻⁹ They have shown that a variety of organic substrates including alcohols and amines can be oxidized to their corresponding aldehydes and nitriles using Pd(II) catalysts and triplet oxygen. This work marks an important, historical step towards greener oxidation reaction conditions. In continuing to improve upon this process, current research endeavors have attempted to shift away from using rare earth transition metals, including biomimetic iron oxo approaches.¹⁰⁻¹² In all of these cases, an electron transfer mediator is used to facilitate reactivity, either directly with oxygen or in a redox process at the catalyst. Though side reactions with an electron transfer mediator can be avoided, eliminating the use of a single electron transfer mediator in aerobic oxidation catalysis would further simplify the catalytic process and reduce overall cost, goals that are favorable in industrial scaling of such reactions.

Some photochemical methods provide a particularly unique route to aerobic oxidation catalysis that does exactly this, namely, through the generation of singlet oxygen ($^1\text{O}_2$) as a redox active, reactive oxygen species (ROS). $^1\text{O}_2$ can be generated from $^3\text{O}_2$ with the use of a photosensitizer (PS). Energy transfer (ET) between $^3\text{O}_2$ and the excited triplet photosensitizer ($^3\text{PS}^*$) has no net exchange of electrons to generate $^1\text{O}_2$ and thus does not require the use of a sacrificial electron donor to regenerate ^1PS .¹³ Using $^1\text{O}_2$ directly for synthetic purposes has been

difficult to realize, with low substrate scopes because of its poor selectivity and transient nature.^{14–}

¹⁶ Finding more efficient ways of utilizing $^1\text{O}_2$ for aerobic oxidation photocatalysis has thus been an ongoing research challenge to the organic chemistry field.

Tellurorhodamine dyes are a unique group of photocatalysts that can both photosensitize and react with $^1\text{O}_2$ to generate an intermediate oxidant that can engage in more selective oxidation reactions. Though initially developed by Detty *et. al.* for photodynamic therapy applications, we have shown that these chromophores can function as aerobic oxidation photocatalysts that can engage in a variety of oxidation chemistries that is quite unique to this system.^{17–21} Tellurorhodamines can be used as photocatalysts in both oxidase (no transfer of O atom) and oxygenase-like reactions (transfer of O atom). Our initial work with tellurorhodamines showed that they can react in an oxidase-like mechanism in which subsequent substitutions of two equivalents of thiols directly to the Te center, followed by reductive elimination gave aromatic disulfides in high yield. More recently, we have used tellurorhodamine dyes as catalysts in the oxidation of silanes and phosphines to their corresponding oxides (oxygenase-like).^{22,23} As exciting as this dual reactivity is, improving tellurorhodamine reactivity in oxidation reactions through synthetic modification has been, until now, entirely unexplored.

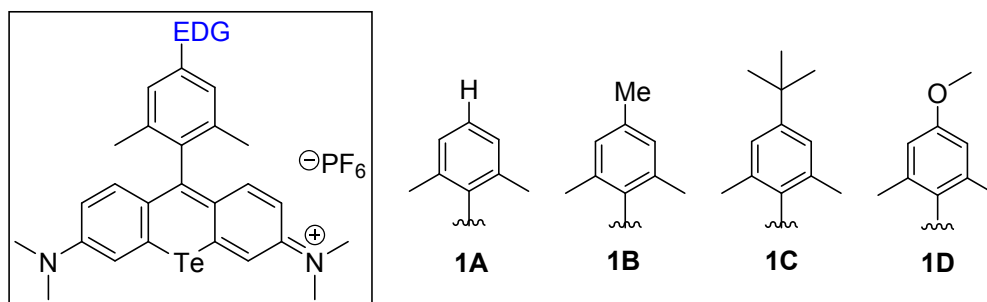
We herein report the synthesis of four tellurorhodamine dye derivatives with varying strength electron donating groups installed on the xylene ring to understand how electronically-driven modifications effect the two individual halves of the catalytic cycle, oxidation of Te(II) to Te(IV) with $^1\text{O}_2$ and reduction of Te(IV) to Te(II) via silane oxidation. We theorized that by influencing the electron density at the reactive center (the tellurium atom), we could later target improved tellurorhodamine design and reactivity towards more challenging oxidation reactions. To study how these functional groups effect oxidation and reduction of the organotellurium, rates of oxidation of Te(II) to Te(IV) and of reduction of Te(IV) to Te(II) were measured and compared. The rates of photooxidation of the four dyes to generate the Te(IV) species with self-sensitized $^1\text{O}_2$ were measured as an isolated step. The rates of reduction for each isolated Te(IV) dye were

then measured via the oxidation methylphenyl silane, the mechanism of which we have described previously.

2 RESULTS AND DISCUSSION

Synthesis of tellurorhodamine derivatives.

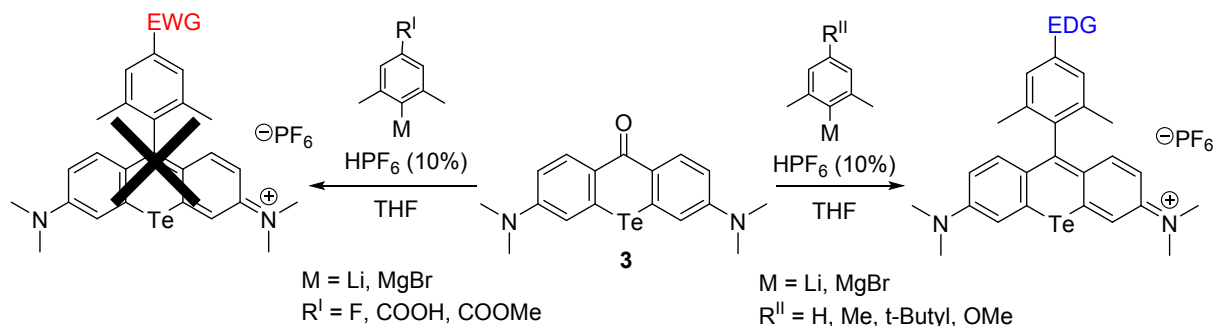
To probe structure-function relationships of tellurorhodamine dyes used in aerobic oxidation photocatalysis, a variety of synthetic targets were chosen that contained substituents on the xylene ring (Scheme 1). Organometallic approaches including organo-magnesium and organo-lithium reagents were used in the carbon-carbon bond forming reaction to couple substituted bromoxylene rings to 3,6-bis-(dimethylamino)-9H-telluroxanthen-9-one (**3**) (Supporting Information, Scheme S1), resulting in moderate to high yields of the desired tellurorhodamine derivatives for EDG-containing xylenes. The dyes were characterized by ^1H , ^{13}C NMR, (Supporting Information Figures S1-S4), and HR-MS (Supporting Information Figures S5-S8).



Scheme 1. Tellurorhodamine derivatives with electron donating substituents on the xylene ring.

Attempts to synthesize derivatives with EWG were unsuccessful. The deactivating nature of EWG located para to the bromine of the bromoxylene starting material, resulted in poor

nucleophilic coupling to **3** (Scheme 2) with no product obtained for derivatives with EWG substitution on the xylene.



Scheme 2. Synthesis of tellurorhodamine derivatives from **3**. Successful synthesis was only accomplished with EDG substituted bromoxylenes.

For example, a solution of 4-bromo-3,5-dimethylbenzoic acid and TMEDA was treated with two equivalents of tertbutyl lithium at $-90\text{ }^{\circ}\text{C}$, which stabilizes the dilithium dianion and discourages formation of the benzophenone self-addition product. Compound **3**, dissolved in anhydrous THF, was then added to the dianion at $-90\text{ }^{\circ}\text{C}$. The mixture was warmed to room temperature, then refluxed for 2 hours. However, only trace amounts of the desired carboxylic acid substituted tellurorhodamine derivative could be detected with mass spectrometry following workup. Similarly low yields were observed for a variety of other EWG substituted bromoxylenes, including 2-bromo-5-fluoro-1,3-dimethylbenzene, 2,3,4,5,6-pentafluorobromobenzene, and methyl 4-bromo-3,5-dimethylbenzoate. These compounds were not isolated.

Synthetic targets with EDG with varying *para*-Hammet parameters (σ_p) were successfully synthesized through bromine-lithium exchange or Grignard reagent formation. **1B**, a dye previously published by our group, contains a methyl substituted xylene (mesityl ring, $\sigma_p = -0.17$). To better compare reactivity of the electron donating groups relative to a baseline, **1A** was synthesized, which has a proton in the 4-position of the xylene ($\sigma_p = 0$). **1C** contains a tert-butyl group on the xylene ($\sigma_p = -0.20$). To confirm successful synthesis and purity, the dyes were

characterized using $^1\text{H}/^{13}\text{C}$ NMR spectroscopies, mass spectrometry, and elemental analysis. Crystal structures were obtained for **1A** and **1B**. Though the synthesis of **1B** was previously accomplished by Detty *et.al.*, our group was the first to successfully obtain a crystal structure of the mesityl tellurorhodamine derivative.

Crystal structures

Crystal structures of **1A**, and **1B** were obtained following recrystallization using the vapor exchange method with acetonitrile and diethyl ether, grown at 11 $^{\circ}\text{C}$ over 2 weeks (Supporting Information Table S1-S12). The visualized structures are shown in Figure 1.

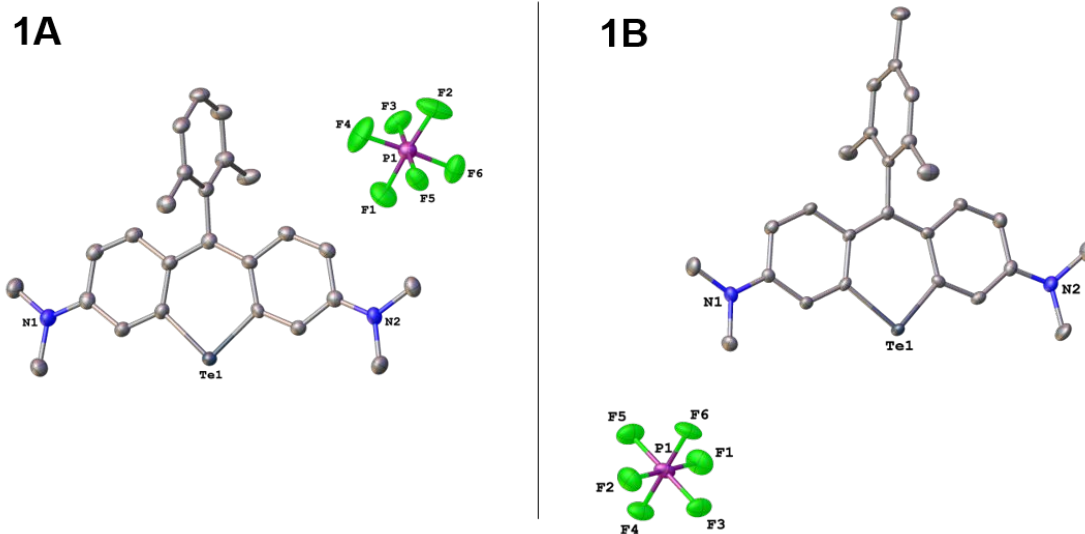


Figure 1. Crystal structures of **1A** (left), **1B** (right) shown with the PF_6 counter anion. Hydrogens are omitted for clarity.

Overall the bonds of interest, namely the Te-C bond lengths and angles do not change significantly between the two structures, indicating that the change in electronics to the Te from the Me xylene substituent is minimal compared to H alone. **1A** and **1B** have the same nearly 90° angle between the xylene moiety and the xanthene core as other literature reports of tellurorhodamine x-ray crystal structures, highlighting the steric strain present in these

molecules.²⁴ For this reason, we believe that even very small increases to the electronegativity of the xanthone through induction will result in changes to photophysical properties and redox reactivity.

Photophysical properties

Photophysical properties of each new dye were determined through UV-vis spectroscopy. Properties of **1A**, **1B**, **1C**, and **1D** and their oxidized forms are compiled in Table 1.

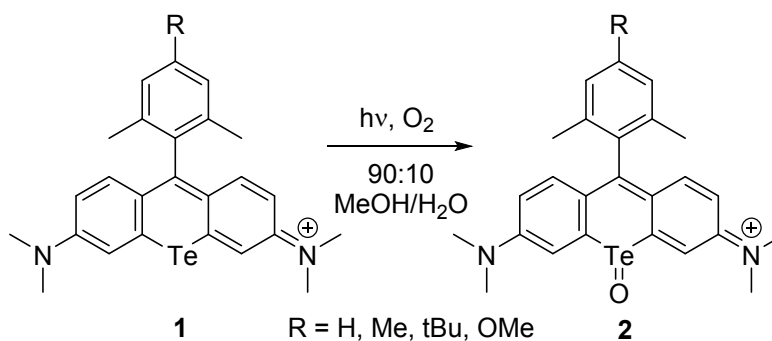
Table 1. Photophysical data for substituted xylene tellurorhodamine derivatives

| Reduced dye | ϵ ($M^{-1} \text{ cm}^{-1}$) ^a | λ_{max} (nm) ^a | Oxidized dye | ϵ ($M^{-1} \text{ cm}^{-1}$) ^b | λ_{max} (nm) ^b |
|-------------------------|--|--|-------------------------|--|--|
| 1A | 150 000 | 599 | 2A | 190 000 | 665 |
| 1B ²² | 86 000 | 598 | 2B ²² | 95 000 | 664 |
| 1C | 80 000 | 595 | 2C | 92 000 | 660 |
| 1D | 82 000 | 596 | 2D | 100 000 | 662 |

^a photophysical data obtained in methanol

^b photophysical data obtained in 1:1 methanol/water

Molar extinction coefficients (ϵ) for the reduced dyes were recorded in methanol (1.0×10^{-5} M). As oxidation slows considerably in the absence of water,²³ ϵ for the oxidized forms of each dye were calculated in 90:10 MeOH/H₂O (1.0×10^{-5} M) following irradiation with a warm white light LED (Scheme 3).



Scheme 3. General reaction for aerobic oxidation of **1A-1D** to **2A-2D** with visible light irradiation.

The absorbance maxima of the reduced form of the dyes ranged from 596-599 nm and the oxidized forms ranged from 660-664 nm (Table 1). An isosbestic point is observed between the spectra of the reduced and oxidized dyes, ranging from 618-622 nm for the series of dyes, indicating that the reduced dyes are directly converted to their oxidized forms via reaction with self-sensitized 1O_2 (Figure 2).

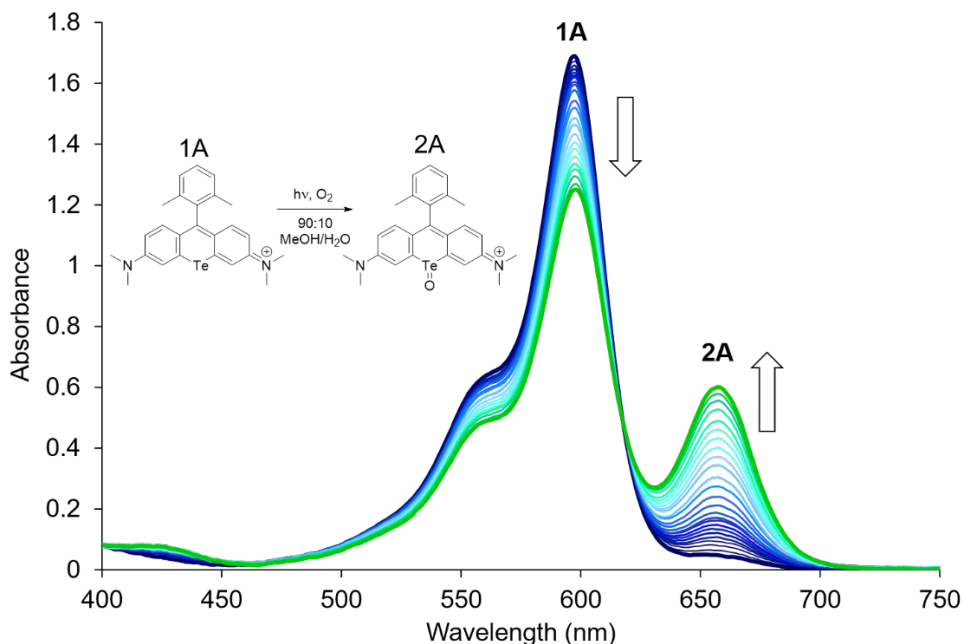


Figure 2. UV-Vis absorption spectra showing the oxidation of **1A** to **2A** with under O_2 in 90:10 MeOH/ H_2O with warm white LED irradiation. Spectra were collected every 10 s for the first 2 min, and then every 30 s for a total of 8.5 min.

Following oxidation, each solution was analyzed with mass spectrometry to confirm the identity of the oxidation products. With each oxidized sample, the mass spectra shifted +16 m/z, indicating the addition of a single oxygen atom (Figure S5-S8).

For both oxidized and reduced compounds, the unsubstituted xylene derivative (**1A/2A**) had a slightly red-shifted absorbance maxima and the largest molar extinction coefficient. When compared to the other dyes, a linear trend emerges between the absorbance maxima and ϵ values with respect to the substituent Hammett constant (σ_p) of the xylene functionality. TD-DFT and molecular orbital surfaces were used to further investigate these trends. Calculations were performed with a CPCM methanol solvent model to simulate experimental conditions. It should be noted that in previous calculations done by our group on tellurorhodamine compounds the SMD solvent model with the methanol dielectric constant was used.²⁵ However, in these cases, using the SMD solvent model lead to larger overestimation of orbital and energy values (though some overestimation is to be expected) of the modified tellurorhodamine analogs, and thus CPCM proved a better fit for this application. Figure 3 shows representations of the frontier molecular orbitals (FMOs) for **1A** and **2A**.

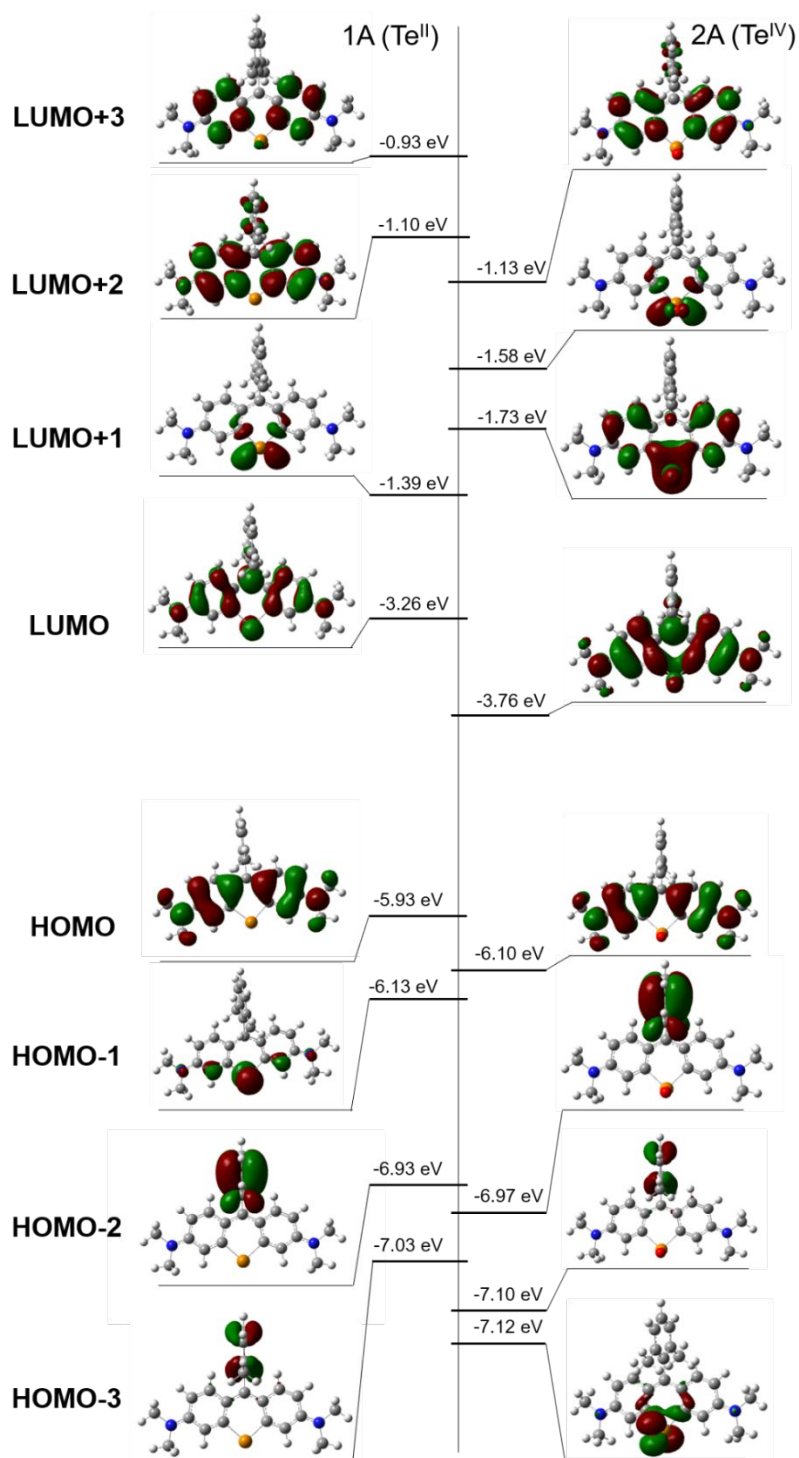


Figure 3. Calculated FMO surfaces for **1A** and **2A**.

1A, **1B**, **1C** and **1D** and their oxidized forms have similarly located frontier molecular orbitals, thus, for simplicity, only the FMOs for **1A** and **2A** are shown (Figure 3). Calculated

absorption maxima and oscillator strengths (f) of the major electronic transition ($f > 0.1$) in the visible region for each dye are shown in Table 1. Calculated λ_{\max} values are shifted from experiment by about 100 nm for both the reduced and oxidized dyes, as expected for TD-DFT calculations, though the trends in absorbance maxima are maintained between experiment and computations with **1A** being most blue shifted, although the differences in computed absorptions are very small, the expected trend is better seen in the changes in the HOMO and LUMO energy levels.

Table 1. Calculated photophysical properties of **1/2A-D** from TD-DFT.

| Reduced dye | λ_{\max} (with f^a) (nm) | HOMO energy (eV) | LUMO energy (eV) | Oxidized dye | λ_{\max} (with f^a) (nm) | HOMO energy (eV) | LUMO energy (eV) |
|-------------|-------------------------------------|------------------|------------------|--------------|-------------------------------------|------------------|------------------|
| 1A | 505 (0.94) | -5.928 | -3.263 | 2A | 559 (0.91) | -6.102 | -3.758 |
| 1B | 504 (0.94) | -5.925 | -3.250 | 2B | 559 (0.91) | -6.093 | -3.745 |
| 1C | 503 (0.93) | -5.920 | -3.249 | 2C | 558 (0.90) | -6.094 | -3.744 |
| 1D | 504 (0.94) | -5.918 | -3.250 | 2D | 559 (0.90) | -6.090 | -3.746 |

^a oscillator strength of HOMO \rightarrow LUMO electronic transition

The electronic transition with the largest oscillator strength for **1A**, **1B**, **1C**, and **1D** is the π - π^* , HOMO to LUMO transition, which are both delocalized across the xanthene and include the tertiary amine lone pairs (Figure 3). The trend in absorption is also observed in the oxidized dyes, where the xanthene based π - π^* transition of **2A**, **2B**, **2C**, and **2D** involves the HOMO and LUMO.

In both experiment and computation, the increase in relative strength of the electron donating xylene substituent resulted in a decreased in λ_{\max} of the reduced dyes. Computations reflect this as an increase in energy of both the HOMO and, to a slightly larger degree, LUMO as

a result of destabilization from increased electron repulsion. This trend is also present in the oxidized dyes. All the oxidized dyes are red-shifted as compared to the reduced dyes, due to a stabilizing effect of the Te(II) to Te(IV) oxidation, lowering the energies of the xanthene-centered HOMO and LUMOs.

Oxidation kinetics of 1A-1D to 2A-2D with self-sensitized 1O_2

The rates of oxidation for the reaction with self-sensitized 1O_2 were determined with UV-Vis spectroscopy for all four dyes and compared. Cuvettes containing the reduced dyes (1.1×10^{-5} M) were purged with O_2 for 60 seconds to saturate the aqueous solvent mixture (Scheme). The solutions were irradiated with stirring and the absorbance at λ_{max} was monitored every 30 seconds. Rates were determined by plotting the natural log of the concentration of the reduced dyes [1A-1D] versus time. Plots of $\ln[1A-1D]$ with the corresponding rates are shown in Figure 4. **1A**, which has a Hammett constant of 0, overall had the fastest rate of oxidation by self-sensitized 1O_2 ($5.23 \pm 0.09 \times 10^{-4} \text{ s}^{-1}$), followed **1B** ($4.82 \pm 0.05 \times 10^{-4} \text{ s}^{-1}$) and **1C** ($4.96 \pm 0.09 \times 10^{-4} \text{ s}^{-1}$). **1D** had the slowest rate of oxidation at $4.10 \pm 0.09 \times 10^{-4} \text{ s}^{-1}$. Plotting the rate of oxidation shows a trend with the Hammett constant of the substituents shown in the insert of Figure 4.

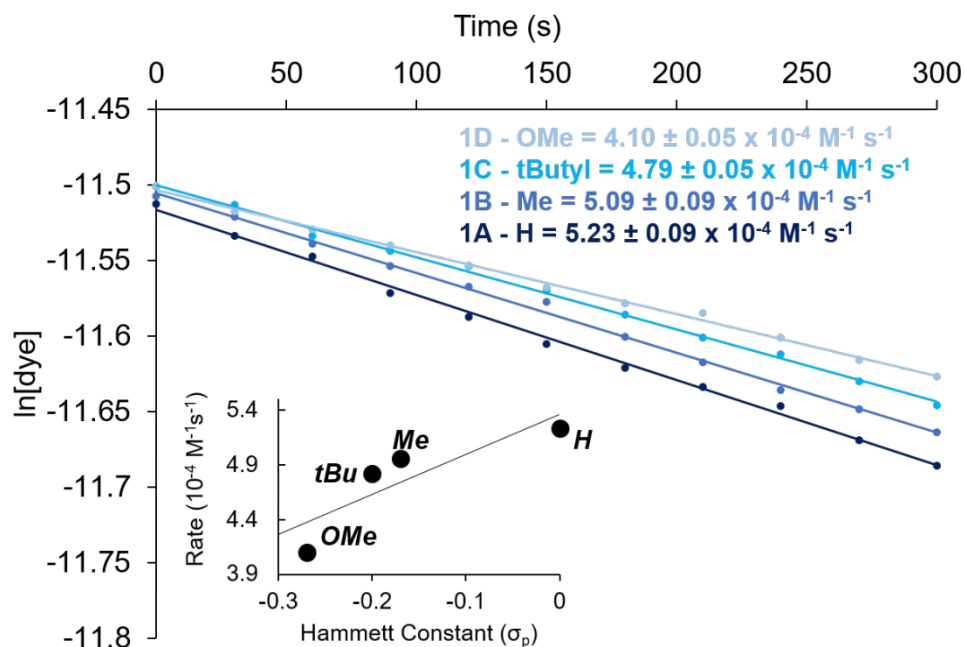


Figure 4. Rates of oxidation of dyes **1A-1D** by self-sensitized $^1\text{O}_2$ with (insert) the rates plotted against the para Hammett Constants for the xylene functionality.

The rates of dye oxidation decrease with more electron donating groups as measured by para Hammett constants. To understand this trend, Hirshfeld populations were calculated using DFT to determine how the electron donating group influences electron density at the tellurium atom. The charges obtained for the Te atom of the reduced dyes were very similar to each other. **1A** has the most electropositive value (0.083), which supports the observed trend that **1A** has the fastest oxidation. However, the positive charge character on the tellurium for **1C**, **1B**, and **1D** was calculated to be very similar (~ 0.081), with variations too small to draw any conclusive results (Supporting Information Table S13)

Reduction kinetics and free energies of methyl diphenylsilane oxidation

Rates of reduction of the dyes were determined by monitoring dye concentration with UV-Vis spectroscopy using our previously published methyl diphenyl silane oxidation reaction (Figure 5 insert).²³ We showed previously that there was a significant dependence on water for this reaction,

wherein the calculated solvent kinetic isotope effect was 17.3 and reactivity slowed 40 fold in the absence of water. In using this model reaction for investigation of the reduction kinetics for **2A-2D** we employed pseudo first order conditions using 100 eq of methyl diphenyl silane (8.4×10^{-4} M) to reduce **2A-2D** (8.4×10^{-6} M) in a 1:1 mixture of MeOH/H₂O.

Dye reduction was monitored by UV-Vis spectroscopy using the absorption maxima of the oxidized dyes at a range of temperatures (10-30 °C). Pseudo first order rates were determined by plotting $\ln[2A-2D]$ versus time. Gibbs energies of silane oxidation for each dye were determined by applying the experimentally observed rates at variable temperatures to the linear Eyring equation to obtain ΔH^\ddagger and ΔS^\ddagger values, which were then used to calculate ΔG^\ddagger .²⁶⁻²⁸ Rates of dye reduction via silane oxidation and the associated experimental ΔH^\ddagger 's, ΔS^\ddagger 's, and ΔG^\ddagger 's with errors are shown in Table 2.

Table 2. Experimental rates, ΔH^\ddagger 's, ΔS^\ddagger 's, and ΔG^\ddagger 's for the reduction of **2A-2D**.

| dye | Rate (10^{-4} s^{-1}) @ 10 °C | Rate (10^{-4} s^{-1}) @ 15 °C | Rate (10^{-4} s^{-1}) @ 20 °C | Rate (10^{-4} s^{-1}) @ 25 °C | Rate (10^{-4} s^{-1}) @ 30 °C | ΔH^\ddagger (kJ) | ΔS^\ddagger ($\text{J}\cdot\text{mol}^{-1}\cdot\text{K}^{-1}$) | ΔG^\ddagger (kcal) |
|-----------|---|---|---|---|---|-----------------------------|---|-------------------------------|
| 2A | 3.7 ± 0.1 | 4.0 ± 0.2 | 5.4 ± 0.1 | 10 ± 0.8 | 16 ± 0.5 | 52.0 ± 2.3 | -69.0 ± 8.0 | 17.4 \pm 0.02 |
| 2B | 6.1 ± 0.4 | 7.4 ± 0.2 | 12 ± 0.6 | 20 ± 0.3 | 23 ± 0.6 | 49.7 ± 1.5 | -72.0 ± 5.0 | 17.0 \pm 0.01 |
| 2C | 7.5 ± 0.5 | 9.7 ± 0.4 | 11 ± 0.6 | 14 ± 1 | 16 ± 0.7 | 25.9 ± 2.4 | -154.0 ± 8.1 | 17.1 \pm 0.01 |
| 2D | 16 ± 2 | 28 ± 1 | 32 ± 1 | 37 ± 2 | 39 ± 0.5 | 26.1 ± 4.2 | -145.4 ± 14.7 | 16.6 \pm 0.06 |

As an example, Figure 5 shows the pseudo-first order rates of reduction of **2A** by methyldiphenyl silane at various temperatures. The insert shows the plot of $1/T$ versus $\ln(k_{2A}/T)$. Rate and Eyring plots for all four dyes are compiled in the Supporting Information Figure S10 & S11.

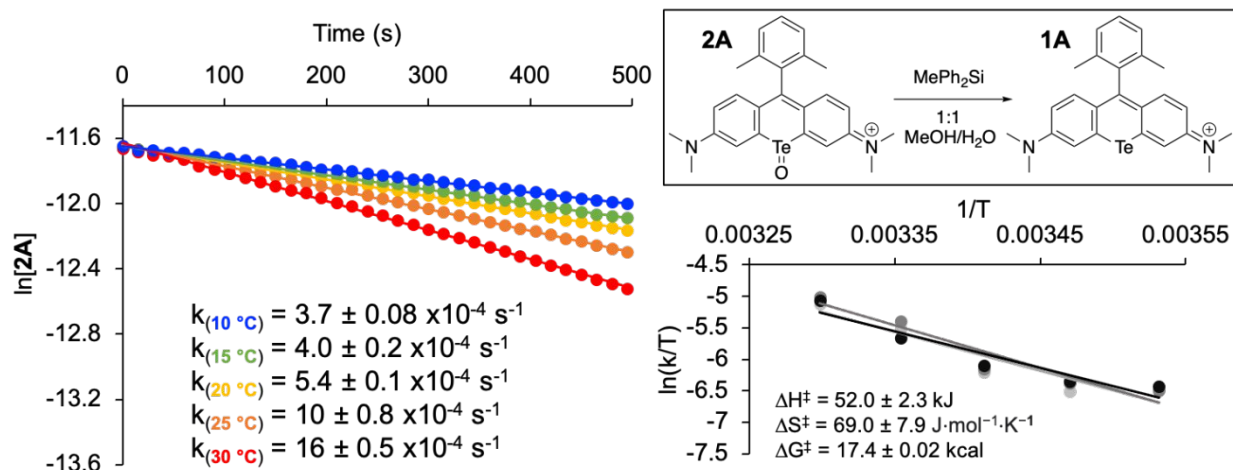


Figure 5. (Left) Pseudo-first order rates of reduction of **2A** at 5 °C increments varying from 10-30 °C. bottom right plot shows the triplicate plots of $1/T$ vs. $\ln(k/T)$ for **2A**, used to calculate experimental values for ΔH^\ddagger , ΔS^\ddagger , and ΔG^\ddagger .

The overall pseudo-first order rates of reduction show the slowest reaction to be **2A**, and the fastest to be **2D** across the temperature range. Considering the Hammett constants for H, Me, tBu, and OMe, the rates correlate linearly with the electron donating nature of the xylene substituent at low temperatures, however, at high temperature that general pattern is broken. At the lowest temperatures (10-20 °C) the individual rates follow a linear pattern, **2D** > **2C** > **2B** > **2A**, wherein the most electron donating xylene substituted dye was a full order of magnitude faster than the other dyes at 10 °C and 15 °C. At the two higher temperatures however, this pattern is broken and instead the rates of silane oxidation are **2D** > **2B** > **2C** > **2A**. Considering that the Hammett constants for Me and tBu only differ by 0.03 and that the electronic effect from the xylene substitutions are purely inductive, the described shift between **2B** and **2C** at higher temperatures does not seem significant to us.

However, with the same reasoning we find it exciting that the inductive electronic effects of the OMe substituent resulted in a ΔG^\ddagger of 16.6 kcal for **2D**, considerably lower than the other dyes. As observed at higher temperatures, ΔG^\ddagger of **2B** and **2C** are very close together (17.0 and 17.1 kcal). The reduction of **2A** with silane had the highest ΔG^\ddagger of 17.4 kcal. Again, considering that the effect of these substituents is exclusively inductive and thus diminished as compared to

electron donation via resonance, a ~ 1 kcal decrease in the Gibbs energy between **2A** and **2D**, the structural difference between them being a mildly electron donating group, showcases the tuneability of these dyes. Based on our computational modeling of the FMO's of **2A**, **2B**, **2C**, and **2D** shown earlier, a similar decrease in the energy of the π^* LUMO was observed with increasing electron withdrawing nature of the xylene substituent, with the lowest energy LUMO belonging to **2D** (Table 1). Thus, decreasing the electron density of the Te-containing conjugated xanthone may lower the energy of the LUMO, making reduction easier.

Though the photophysical effect of changes to the tellurorhodamine dye structure have been explored^{18,21}, this is the first study to investigate how attaching increasingly electron donating substituents to the xylene group changes reactivity. Improving our understanding of how to change the reactivity of these dyes is crucial to their continued improvement towards aerobic oxidation reactions.

3 CONCLUSION

We report the synthesis and characterization of multiple tellurorhodamine derivatives with the target goal of determining how the introduction of different EDG substituents effects reactivity in redox reactions. Dyes **1A**, **1B**, **1C**, and **1D** contain increasingly strong EDG in the para position of the 9-xylene moiety, which were achieved via bromine-lithium exchange and addition to tellurone **3**. Attempts at generating tellurorhodamine analogs with EWG substituents on the xylene failed due to ring deactivation caused by the EWG groups themselves, which merits further investigations into other approaches towards this functional group tolerant synthetic methods.

In the oxidation half reaction with self-sensitized $^1\text{O}_2$, **1A** had the fastest rate of oxidation, followed by **1B**, **1C**, and **1D**. Mass spectrometry was used to identify the oxidation products as telluroxides **2A**, **2B**, **2C**, **2D**. Following their formation, the telluroxides were reduced with methyl-diphenyl silane and their rates determined at a range of temperatures, which were used to

calculate reaction thermodynamics. Rates of reduction via silane oxidation were determined at a variety of temperatures in order to measure both kinetic and thermodynamic components of dye reduction. The results showed that **2D** had the smallest energy barrier to silane oxidation compared to the other dyes. When comparing these kinetic and thermodynamic values to Hammett parameters, a linear increase in rate with increasing substituent electron withdrawing nature was observed at low temperatures, and non-linearity at high temperatures. Based on our findings we determined the inductive effect of increased electronegativity of the xylene was enough to change the electronics of the Te-containing xanthone, resulting in increased reduction reactivity. These preliminary results show the potential for more dramatic changes in aerobic oxidation reactivity with continued exploration of tellurorhodamine dye modifications.

4 EXPERIMENTAL

Preparation of 3,6-Bis(dimethylamino)-9-(2,6-dimethylphenyl)-9H-telluroxanthen-9-ylum hexafluorophosphate (1A).

2-Bromo-1,3-dimethylbenzene (0.17 mL, 1.27 mmol) was added to a stirred suspension of magnesium (100 mg) and iodine (2 chips) in anhydrous THF (6 mL). The mixture was stirred at ambient temperature for 3 h (visible consumption of magnesium turnings) and the resulting Grignard solution was transferred via cannula to a stirred suspension of 3,6-bis-(dimethylamino)-9H-telluroxanthen-9-one (**4**) (50 mg, 0.127 mmol) in anhydrous THF (2.5 mL). The resulting mixture was heated at reflux overnight (16 h), cooled to ambient temperature, and quenched by the addition of glacial acetic acid (1 mL). The stir bar was removed and the blue solution was poured into 50 mL of 10% (by weight) aqueous HPF_6 and allowed to stand without stirring for 12 h. The resulting precipitate was collected via filtration and washed with water (50 mL) and diethyl ether (100 mL). The resulting blue solid was recrystallized via vapor exchange (acetonitrile solvent, diethyl ether antisolvent). The resulting metallic green crystals were collected via vacuum

filtration and rinsed with diethyl ether to give 21.1 mg (26.3%) of **1A**. $^1\text{H NMR}$ [600 MHz, CD_2Cl_2] δ 7.84 (s, 2H, $J = 2.68$), 7.74 (d, 2H, $J = 9.70$), 7.36 (t, 1H, $J = 7.67$), 7.22 (d, 2H, $J = 7.67$), 6.87 (d, 2H, $J=2.68, 9.77$), 3.17 (s, 12H), 1.82 (s, 6H). LCMS m/z 485.1231 (calcd for $\text{C}_{25}\text{H}_{27}\text{N}_2\text{Te}^+$ 485.1231).

Preparation of 3,6-Bis(dimethylamino)-9-(4-tertbutyl-2,6-dimethylphenyl)-9H-telluroxanthen-9-ylidium hexafluorophosphate (1C).

N-butyl lithium (1.1 M, 1.27 mmol) was added dropwise to a stirring solution of TMEDA (0.2 mL, 1.27 mmol) and 2-bromo-5-tert-butyl-1,3-dimethylbenzene (0.15 g, 1.27 mmol) in anhydrous THF (6 mL) that had been cooled to $-78\text{ }^\circ\text{C}$. The resulting solution was stirred at $-78\text{ }^\circ\text{C}$ for 15 minutes. The solution was removed from cooling and immediately canula transferred to a stirring solution of 3,6-bis-(dimethylamino)-9H-telluroxanthen-9-one (**4**) (50 mg, 0.127 mmol) in anhydrous THF (2.5 mL). Upon addition, telluroxanthone solution changed in color from opaque yellow/green to clear orange. Following the canula transfer, the resulting mixture was allowed to stir for 30 minutes and then quenched with 0.5 mL of acetic acid. The resulting solution stirred open to air for 1 hour, resulting in a color change from cloudy forest green immediately following acetic acid addition to royal blue. The stir bar was removed and the blue solution was poured into 50 mL of 10% (by weight) aqueous HPF_6 and allowed to stand without stirring for 12 h. The precipitate was collected via vacuum filtration and rinsed with water (50 mL) and diethyl ether (100 mL). The resulting blue solid was loaded onto 5 mL basic alumina and column purified on alumina. Unreacted **4** (yellow) was eluted first with 100% DCM, followed by ethanol to remove the product. After concentration in vacuo, the resulting blue oil was recrystallized via vapor exchange (acetonitrile solvent, diethyl ether antisolvent). The resulting dark green crystals were collected via vacuum filtration and rinsed with diethyl ether to give 19.8 mg (24.8%) of **1C**. $^1\text{H NMR}$ [600 MHz, CD_2Cl_2] δ 7.50 (s, 2 H, $J = 2.77$), 7.18 (d, 2 H, $J = 9.80$), 7.12 (s, 2 H), 6.64 (d, 2 H, $J = 2.77, 9.82$), 2.97(s, 12H), 1.63 (s, 6H), 1.19 (s, 9H). $^{13}\text{C NMR}$ [400 MHz, CD_3OD] δ 167.17, 154.39, 153.58, 138.58, 137.43,

136.46, 126.08, 120.63, 118.28, 117.31, 101.23, 31.78, 24.21, 19.97. LCMS m/z 541.1854 (calcd for $C_{29}H_{35}N_2Te^+$ 541.1850).

Preparation of 3,6-Bis(dimethylamino)-9-(4-methoxy-2,6-dimethylphenyl)-9H-telluroxanthen-9-ylidium hexafluorophosphate (1D).

2-Bromo-5-methoxy-1,3-dimethylbenzene (0.31 mL, 1.90 mmol) was added to a stirred suspension of magnesium (100 mg) and iodine (2 chips) in anhydrous THF (4 mL). The mixture was heated to initiate Grignard formation, cooled to ambient temperature following color change from clear yellow to opaque white, and then stirred for 2 h (visible consumption of magnesium turnings). The resulting Grignard solution was transferred via cannula to a stirred suspension of 3,6-bis-(dimethylamino)-9H-telluroxanthen-9-one (**4**) (50 mg, 0.127 mmol) in anhydrous THF (2.5 mL). The resulting mixture was heated at reflux overnight (18 h), cooled to ambient temperature, and quenched by the addition of glacial acetic acid (0.5 mL). The stir bar was removed and the blue solution was poured into 50 mL of 10% (by weight) aqueous HPF_6 and allowed to stand without stirring for 12 h. The resulting precipitate was collected via filtration and washed with water (50 mL) and diethyl ether (100 mL). The resulting purple solid was recrystallized via vapor exchange (acetonitrile solvent, diethyl ether antisolvent). The resulting metallic purple crystals were collected via vacuum filtration and rinsed with diethyl ether to give 37.5 mg (44.7 %) of **1D**. 1H NMR [400 MHz, $CDCl_3$] δ 7.61 (s, 2 H, $J = 2.66$), 7.52 (d, 2 H, $J = 9.72$), 6.76 (s, 2 H), 6.74 (d, 2 H, $J = 2.65, 11.07$), 3.89 (s, 3H), 3.23 (s, 12H), 1.83 (s, 6H). ^{13}C NMR [400 MHz, $CDCl_3$] δ 165.09, 159.87, 152.25, 139.53, 139.37, 130.85, 121.77, 115.92, 115.45, 113.44, 55.47, 40.69, 20.11 LCMS m/z 515.1328 (calcd for $C_{26}H_{29}N_2TeO^+$ 515.1342).

Recrystallization of 1B.

The synthesis of **1B** is described in reference 23. For preparation for crystal structure analysis, the 10 mg of the green solid collected via vacuum filtration was recrystallized via vapor exchange

(acetonitrile solvent, diethyl ether antisolvent) at 4 °C. The resulting metallic green needles (4.0 mg) were collected via vacuum filtration and rinsed portion wise first with diethyl ether, followed by water.

Crystal structure determination (1A)

A crystal of **1A** (0.092 x 0.082 x 0.016 mm³) was placed onto a thin glass optical fiber or a nylon loop and mounted on a Rigaku XtaLAB Synergy-S Dualflex diffractometer equipped with a HyPix-6000HE HPC area detector for data collection at 100.00(10) K. The full data collection was carried out using a PhotonJet (Cu) X-ray source with frame times of 0.36 and 1.42 seconds and a detector distance of 31.2 mm. Series of frames were collected in 0.50° steps in w at different 2θ , k , and f settings. After the intensity data were corrected for absorption, the final cell constants were calculated from the xyz centroids of 30698 strong reflections from the actual data collection after integration. The structure was solved using SHELXT³³ and refined using SHELXL.³⁴ The space group $P-1$ was determined based on intensity statistics, (triclinic, $Z=2$, $a=7.8985(2)$, $b=13.2724(2)$, $c=14.3100(2)$ Å, $U=1352.64(5)$ Å³). Most or all non-hydrogen atoms were assigned from the solution. Full-matrix least squares / difference Fourier cycles were performed which located any remaining non-hydrogen atoms. All non-hydrogen atoms were refined with anisotropic displacement parameters. All hydrogen atoms were placed in ideal positions and refined as riding atoms with relative isotropic displacement parameters. The final full matrix least squares refinement converged to $R1 = 0.0375$ (F^2 , $I > 2s(I)$) and $wR2 = 0.0999$ (F^2 , all data). CCDC deposition #2216548.

Crystal structure determination (1B)

A crystal of **1B** (0.183 x 0.133 x 0.125 mm³) was placed onto a thin glass optical fiber or a nylon loop and mounted on a Rigaku XtaLAB Synergy-S Dualflex diffractometer equipped with a HyPix-6000HE HPC area detector for data collection at 99.99(10) K. The full data collection was carried

out using a PhotonJet (Cu) X-ray source with frame times of 0.05 and 0.17 seconds and a detector distance of 31.2 mm. Series of frames were collected in 0.50° steps in w at different 2θ , k , and f settings. After the intensity data were corrected for absorption, the final cell constants were calculated from the xyz centroids of 26847 strong reflections from the actual data collection after integration. The structure was solved using SHELXT³³ and refined using SHELXL.³⁴ The space group $P2_1/c$ was determined based on systematic absences (monoclinic, $Z=14$, $a=8.0869(1)$, $b=20.1974(2)$, $c=15.9300(2)$ Å, $U=2558.34(5)$ Å³). Most or all non-hydrogen atoms were assigned from the solution. Full-matrix least squares / difference Fourier cycles were performed which located any remaining non-hydrogen atoms. All non-hydrogen atoms were refined with anisotropic displacement parameters. All hydrogen atoms were placed in ideal positions and refined as riding atoms with relative isotropic displacement parameters. The final full matrix least squares refinement converged to $R1 = 0.0357$ (F^2 , $I > 2s(I)$) and $wR2 = 0.0983$ (F^2 , all data). CCDC deposition #2216849.

Photooxidation of 1A, 1B, 1C, and 1D

Solutions of **1A**, **1B**, **1C**, and **1D** (1.1×10^{-5} M) in 90:10 MeOH/H₂O were purged with O₂ for 60 seconds in the dark, sealed, and then irradiated with white light LEDs at room temperature with stirring and monitored by UV-vis absorption (LED spectrum is shown in Supporting Information Figure S9). Spectra were collected every 10 s for the first 2 min, and then every 30 s for a total of 8.5 min. Photooxidation kinetics are an average of triplication measurements.

Reduction of 2A, 2B, 2C, and 2D by Ph₂MeSiH.

Stock solutions of **1A**, **1B**, **1C** and **1D** (1.0×10^{-5} M) in 1:1 MeOH/H₂O were irradiated with white light LEDs and monitored by UV-vis absorption to convert the dyes to their oxidized forms via reaction with self-sensitized ¹O₂. When the absorbance maxima for **2A**, **2B**, **2C**, and **2D** persisted, the samples were stored in the dark for no more than 1 hour before reduction kinetics were

performed. Solutions of **2A**, **2B**, **2C**, and **2D** (8.4×10^{-6} M) in 1:1 MeOH/H₂O were prepared from the stock solutions. 10.5 μ L (8.4×10^{-4} M) of a stock solution of Ph₂MeSiH (0.24 M) in dry, degassed MeOH was spiked into the dye solutions, sealed, and the gradual decrease of the absorbance maxima of **2A**, **2B**, **2C**, and **2D** monitored with UV-vis. Reduction kinetics were determined in triplicate for a range of temperatures (10, 15, 20, 25, and 30 °C). Experimental Gibbs free energies (G_{exp}) were calculated by plotted using an Eyring plot ($1/T$ vs. $\ln(k/T)$).

Computational details.

Calculations were done using Gaussian09,³⁵ and results were visualized using GaussView05.³⁶ All structures were optimized using the B3LYP^{37–39} level of theory with the 6-31+G(d)^{40–42} basis set for all light atoms and LanL2DZ^{43–45} for Te, with the inclusion of CPCM (methanol) solvent model. Hirshfeld charge population analyses were calculated from optimized geometries.^{46,47}

5 Conflicts of Interest

There are no conflicts to declare

6 Acknowledgments

This work was funded by the American National Science Foundation, Directorate for Mathematical and Physical Science, Division of Chemistry, award #1800599. Funding was also provided from the Portland State University Faculty Development Grant. The National Science Foundation is acknowledged for support of the BioAnalytical Mass Spectrometry Facility at PSU (MRI 1828573). We acknowledge Dr. William Brennessel from the University of Rochester for the single crystal XRD data.

7 REFERENCES

- (1) Anastas, P. T.; Kirchhoff, M. M.; Williamson, T. C. Catalysis as a Foundational Pillar of Green Chemistry. *Appl. Catal. A Gen.* **2001**, *221* (1–2), 3–13.
[https://doi.org/10.1016/S0926-860X\(01\)00793-1](https://doi.org/10.1016/S0926-860X(01)00793-1).
- (2) Lévesque, F.; Seeberger, P. H. Highly Efficient Continuous Flow Reactions Using Singlet Oxygen as a “Green” Reagent. *Org. Lett.* **2011**, *13* (19), 5008–5011.
<https://doi.org/10.1021/ol2017643>.
- (3) Campbell, A. N.; Stahl, S. S. Overcoming the “Oxidant Problem”: Strategies to Use O₂ as the Oxidant in Organometallic C–H Oxidation Reactions Catalyzed by Pd (and Cu). *Acc. Chem. Res.* **2012**, *45* (6), 851–863. <https://doi.org/10.1021/ar2002045>.
- (4) Smidt, J.; Hafner, W.; Jira, R.; Sedlmeier, J.; Sieber, R.; Rüttinger, R.; Kojer, H. Katalytische Umsetzungen von Olefinen an Platinmetall-Verbindungen Das Consortium-Verfahren Zur Herstellung von Acetaldehyd. *Angew. Chemie* **1959**, *71* (5), 176–182.
<https://doi.org/10.1002/ange.19590710503>.
- (5) Smidt, J.; Hafner, W.; Jira, R.; Sieber, R.; Sedlmeier, J.; Sabel, A. Olefinoxydation Mit Palladiumchlorid-Katalysatoren. *Angew. Chemie* **1962**, *74* (3), 93–102.
<https://doi.org/10.1002/ange.19620740302>.
- (6) Iosub, A. V.; Stahl, S. S. Palladium-Catalyzed Aerobic Dehydrogenation of Cyclic Hydrocarbons for the Synthesis of Substituted Aromatics and Other Unsaturated Products. *ACS Catal.* **2016**, *6* (12), 8201–8213. <https://doi.org/10.1021/acscatal.6b02406>.
- (7) Steinhoff, B. a.; Stahl, S. S. Ligand-Modulated Palladium Oxidation Catalysis: Mechanistic Insights into Aerobic Alcohol Oxidation with the Pd(OAc)₂/Pyridine Catalyst

- System. *Org. Lett.* **2002**, *4* (23), 4179–4181. <https://doi.org/10.1021/ol026988e>.
- (8) Stahl, S. S. Palladium-Catalyzed Oxidation of Organic Chemicals with O₂. *Science*. **2005**, *309* (5742), 1824–1826. <https://doi.org/10.1126/science.1114666>.
- (9) Stahl, S. S.; Thorman, J. L.; Nelson, R. C.; Kozee, M. A. Oxygenation of Nitrogen-Coordinated Palladium(0): Synthetic, Structural, and Mechanistic Studies and Implications for Aerobic Oxidation Catalysis. *J. Am. Chem. Soc.* **2001**, *123* (29), 7188–7189. <https://doi.org/10.1021/ja015683c>.
- (10) Liu, J.; Guðmundsson, A.; Bäckvall, J. E. Efficient Aerobic Oxidation of Organic Molecules by Multistep Electron Transfer. *Angew. Chemie - Int. Ed.* **2021**, *60* (29), 15686–15704. <https://doi.org/10.1002/anie.202012707>.
- (11) Jiang, X.; Liu, J.; Ma, S. Iron-Catalyzed Aerobic Oxidation of Alcohols: Lower Cost and Improved Selectivity. *Org. Process Res. Dev.* **2019**, *23* (5), 825–835. <https://doi.org/10.1021/acs.oprd.8b00374>.
- (12) Li, S.; Li, H.; Tung, C. H.; Liu, L. Practical and Selective Bio-Inspired Iron-Catalyzed Oxidation of Si-H Bonds to Diversely Functionalized Organosilanols. *ACS Catal.* **2022**, *12* (15), 9143–9152. <https://doi.org/10.1021/acscatal.2c02678>.
- (13) Arnold, S. J.; Kubo, M.; Ogryzlo, E. A. Relaxation and Reactivity of Singlet Oxygen; 1968; pp 133–142. <https://doi.org/10.1021/ba-1968-0077.ch070>.
- (14) Ghogare, A. A.; Greer, A. Using Singlet Oxygen to Synthesize Natural Products and Drugs. *Chem. Rev.* **2016**, *116* (17), 9994–10034. <https://doi.org/10.1021/acs.chemrev.5b00726>.
- (15) Foote, C. S.; Dzakpasu, A. A.; H.-P. Lin, J. Chemistry of Singlet Oxygen. XX. Mechanism

- of the Sensitized Photooxidation of Enamines. *Tetrahedron Lett.* **1975**, *16* (14), 1247–1250. [https://doi.org/10.1016/S0040-4039\(00\)72109-5](https://doi.org/10.1016/S0040-4039(00)72109-5).
- (16) DeRosa, M. C.; Crutchley, R. J. Photosensitized Singlet Oxygen and Its Applications. *Coord. Chem. Rev.* **2002**, *233–234*, 351–371. [https://doi.org/10.1016/S0010-8545\(02\)00034-6](https://doi.org/10.1016/S0010-8545(02)00034-6).
- (17) Kryman, M. W.; Schamerhorn, G. a.; Yung, K.; Sathyamoorthy, B.; Sukumaran, D. K.; Ohulchanskyy, T. Y.; Benedict, J. B.; Detty, M. R. R. Organotellurium Fluorescence Probes for Redox Reactions: 9-Aryl-3,6-Diaminotelluroxanthylum Dyes and Their Telluroxides. *Organometallics* **2013**, *32*, 4321–4333.
- (18) Davies, K. S.; Linder, M. K.; Kryman, M. W.; Detty, M. R. Extended Rhodamine Photosensitizers for Photodynamic Therapy of Cancer Cells. *Bioorganic Med. Chem.* **2016**, *24* (17), 3908–3917. <https://doi.org/10.1016/j.bmc.2016.05.033>.
- (19) Detty, M. R.; Merkel, P. B. Chalcogenapyrylium Dyes as Potential Photochemotherapeutic Agents. Solution Studies of Heavy Atom Effects on Triplet Yields, Quantum Efficiencies of Singlet Oxygen Generation, Rates of Reaction with Singlet Oxygen, and Emission Quantum Yields. *J. Am. Chem. Soc.* **1990**, *112* (10), 3845–3855. <https://doi.org/10.1021/ja00166a019>.
- (20) Detty, M. R.; Friedman, A. E.; Oseroff, A. R. A Mechanism for the Oxidation of Glutathione to Glutathione Disulfide with Organotellurium(IV) and Organoselenium(IV) Compounds. A Stepwise Process with Implications for Photodynamic Therapy and Other Oxidative Chemotherapy. *J. Org. Chem.* **1994**, No. 59, 8245–8250.
- (21) Kryman, M. W.; Schamerhorn, G. A.; Hill, J. E.; Calitree, B. D.; Davies, K. S.; Linder, M. K.; Ohulchanskyy, T. Y.; Detty, M. R. Synthesis and Properties of Heavy Chalcogen

- Analogues of the Texas Reds and Related Rhodamines. *Organometallics* **2014**, *33* (10), 2628–2640. <https://doi.org/10.1021/om500346j>.
- (22) Lutkus, L. V.; Rettig, I.; Davies, K. S.; Hill, J. E.; Lohman, J. E.; Eskew, M. W.; Detty, M. R.; McCormick, T. M. Photocatalytic Aerobic Thiol Oxidation with a Self-Sensitized Tellurorhodamine Chromophore. *Organometallics* **2017**, *36* (14), 2588–2596. <https://doi.org/10.1021/acs.organomet.7b00166>.
- (23) Rettig, I. D.; Van, J.; Brauer, J. B.; Luo, W.; McCormick, T. M. Tellurorhodamine Photocatalyzed Aerobic Oxidation of Organo-Silanes and Phosphines by Visible-Light. *Dalt. Trans.* **2019**, *48* (17), 5665–5673. <https://doi.org/10.1039/c9dt00487d>.
- (24) Calitree, B.; Donnelly, D. J.; Holt, J. J.; Gannon, M. K.; Nygren, C. L.; Sukumaran, D. K.; Autschbach, J.; Detty, M. R. Tellurium Analogues of Rosamine and Rhodamine Dyes: Synthesis, Structure, ¹²⁵Te NMR, and Heteroatom Contributions to Excitation Energies. *Organometallics* **2007**, *26* (25), 6248–6257. <https://doi.org/10.1021/om700846m>.
- (25) Marenich, A. V.; Cramer, C. J.; Truhlar, D. G. Universal Solvation Model Based on Solute Electron Density and on a Continuum Model of the Solvent Defined by the Bulk Dielectric Constant and Atomic Surface Tensions. *J. Phys. Chem. B* **2009**, *113* (18), 6378–6396. <https://doi.org/10.1021/jp810292n>.
- (26) Eyring, H. The Activated Complex in Chemical Reactions. *J. Chem. Phys.* **1935**, *3* (2), 107–115. <https://doi.org/10.1063/1.1749604>.
- (27) Rooney, J. J. Eyring Transition-State Theory and Kinetics in Catalysis. *J. Mol. Catal. A Chem.* **1995**, *96* (1), L1–L3. [https://doi.org/http://dx.doi.org/10.1016/1381-1169\(94\)00054-9](https://doi.org/http://dx.doi.org/10.1016/1381-1169(94)00054-9).

- (37) Becke, A. D. A New Mixing of Hartree-Fock and Local-Density-Functional Theories. *J. Chem. Phys.* **1993**, *98* (2), 1372–1377. <https://doi.org/10.1063/1.464304>.
- (38) Lee, C.; Yang, W.; Parr, R. G. *Development of the Colle-Salvetti Correlation-Energy Formula into a Functional of the Electron Density*; 1988; Vol. 37, pp 785–789. <https://doi.org/10.1103/PhysRevB.37.785>.
- (39) Miehlich, B.; Savin, A.; Stoll, H.; Preuss, H. Results Obtained with the Correlation Energy Density Functionals of Becke and Lee, Yang and Parr. *Chem. Phys. Lett.* **1989**, *157* (3), 200–206. [https://doi.org/10.1016/0009-2614\(89\)87234-3](https://doi.org/10.1016/0009-2614(89)87234-3).
- (40) Hehre, W. J.; Ditchfield, R.; Radom, L.; Pople, J. A. Molecular Orbital Theory of the Electronic Structure of Organic Compounds. V. Molecular Theory of Bond Separation. *J. Am. Chem. Soc.* **1970**, *92* (16), 4796–4801. <https://doi.org/10.1021/ja00719a006>.
- (41) Radom, L.; Hehre, W. J.; Pople, J. A. Molecular Orbital Theory of the Electronic Structure of Organic Compounds. VII. A Systematic Study of Energies, Conformations, and Bond Interactions. *J. Am. Chem. Soc.* **1971**, *93* (2), 289–300. <https://doi.org/10.1021/ja00731a001>.
- (42) Hariharan, P. C.; Pople, J. A. The Influence of Polarization Functions on Molecular Orbital Hydrogenation Energies. *Theor. Chim. Acta* **1973**, *28* (3), 213–222. <https://doi.org/10.1007/BF00533485>.
- (43) Wadt, W. R.; Hay, P. J. Ab Initio Effective Core Potentials for Molecular Calculations. Potentials for Main Group Elements Na to Bi. *J. Chem. Phys.* **1985**, *82* (1), 284–298. <https://doi.org/10.1063/1.448800>.
- (44) Hay, P. J.; Wadt, W. R. *Ab Initio* Effective Core Potentials for Molecular Calculations.

- Potentials for K to Au Including the Outermost Core Orbitals. *J. Chem. Phys.* **1985**, *82* (1), 299–310. <https://doi.org/10.1063/1.448975>.
- (45) Hay, P. J.; Wadt, W. R. Ab Initio Effective Core Potentials for Molecular Calculations. Potentials for the Transition Metal Atoms Sc to Hg. *J. Chem. Phys.* **1985**, *82* (1), 270–283. <https://doi.org/10.1063/1.448799>.
- (46) Hirshfeld, F. L. Bonded-Atom Fragments for Describing Molecular Charge Densities. *Theor. Chim. Acta* **1977**, *44* (2), 129–138. <https://doi.org/10.1007/BF00549096>.
- (47) De Proft, F.; Van Alsenoy, C.; Peeters, A.; Langenaeker, W.; Geerlings, P. Atomic Charges, Dipole Moments, and Fukui Functions Using the Hirshfeld Partitioning of the Electron Density. *J. Comput. Chem.* **2002**, *23* (12), 1198–1209. <https://doi.org/10.1002/jcc.10067>.